

AD-A184 682

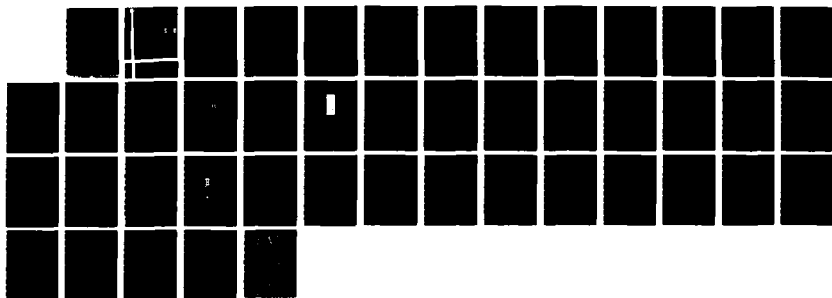
THE INFILTRATION KINETICS OF ALUMINUM IN SILICON  
CARBIDE COMPACTS(U) COLORADO SCHOOL OF MINES GOLDEN  
CENTER FOR WELDING RESEARCH G R EDWARDS ET AL JUL 87  
MT-CWR-087-032 N00014-85-K-0451

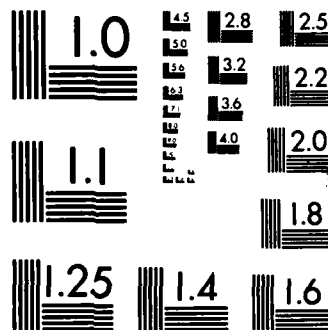
1/1

UNCLASSIFIED

F/G 11/4

NL





MICROCOPY RESOLUTION TEST CHART  
NATIONAL BUREAU OF STANDARDS-1963-A

AD-A184 682

FILE COPY

12

MT-CWR-087-032

ANNUAL REPORT

The Infiltration Kinetics of Aluminum in Silicon Carbide Compacts

Submitted to:

Dr. Steven Fishman  
Office of Naval Research  
800 North Quincy Street  
Arlington, Virginia

DTIC  
ELECTE  
SEP 14 1987  
S D

Submitted by:

Glen R. Edwards and David L. Olson  
Center for Welding Research  
Colorado School of Mines  
Golden, Colorado 80401

This program is supported by the Strategic Defense  
Initiative Office/Innovative Science and Technology  
Under ONR Contract Number N00014-85-K-0451

July, 1987

DISTRIBUTION STATEMENT A

Approved for public release;  
Distribution Unlimited

# TABLE OF CONTENTS

	<u>PAGE</u>
TABLE OF CONTENTS . . . . .	i
LIST OF FIGURES . . . . .	ii
LIST OF TABLES . . . . .	iii
1.0 INTRODUCTION . . . . .	1
2.0 DIMENSIONLESS SOLUTION FOR CAPILLARY RISE - WETTING SYSTEM . . . . .	2
3.0 TUBE BUNDLE/CAPILLARY RISE EXPERIMENTS (NON-WETTING SYSTEM) . . . . .	5
3.1 <u>Static Measurements</u> . . . . .	7
3.2 <u>Dynamic Infiltration Rate Measurements</u> . . . . .	9
4.0 POROUS COMPACT - NON-WETTING SYSTEM . . . . .	13
4.1 <u>Theoretical Model</u> . . . . .	13
4.2 <u>Experimental Methodology</u> . . . . .	17
4.3 <u>Body Characterization</u> . . . . .	19
4.4 <u>Infiltration Kinetics</u> . . . . .	25
4.4.1 <u>Procedure</u> . . . . .	25
4.4.2 <u>Results and Discussion</u> . . . . .	27
4.4.3 <u>Conclusions</u> . . . . .	35
5.0 FUTURE WORK . . . . .	37
5.1 <u>Capillary/Tube Bundle Experiments</u> . . . . .	37
5.2 <u>Porous Compact Experiments</u> . . . . .	38
6.0 ACKNOWLEDGMENTS . . . . .	38
7.0 REFERENCES . . . . .	39

# LIST OF FIGURES

FIGURE		PAGE
1	Schematic of forces balance for capillary rise . . . . .	3
2	Capillary rise (non-wetting) . . . . .	6
3	Wetting tendency ( $\gamma_{LV} \cos \theta$ ) versus temperature for various aluminum alloys on SiC . . . . .	8
4	Schematic of experimental apparatus for capillary rise . . . . .	12
5	Schematic of porous compact sample geometry . . . . .	14
6	Plot of $1/2 P_g (P_g + 2 P_o)$ versus flow rate for green SiC compact (100 grit) . . . . .	23
7	Schematic of experimental apparatus for porous compact . . . . .	26
8	Infiltration distance versus time for aluminum in SiC at 670°C and 69 kPa . . . . .	28
9	Infiltration distance versus time for aluminum in SiC at 670°C and 90 kPa . . . . .	29
10	Infiltration distance versus time for aluminum in SiC at 663°C and 98 kPa . . . . .	30
11	Infiltration distance versus time for aluminum-1 wt % silicon in SiC at 670°C and 90 kPa . . . . .	31
12	Infiltration distance versus time for aluminum-1 wt % Mg in SiC at 670°C and 90 kPa . . . . .	32
13	Infiltration distance versus time for aluminum-1 wt % Si in SiC at 660°C and 98 kPa . . . . .	33



Accession For	
NTIS CRA&I	<input checked="" type="checkbox"/>
DTIC TAB	<input type="checkbox"/>
Unannounced	<input type="checkbox"/>
Justification	
By <i>per ltr.</i>	
Distribution	
Availability Codes	
Dnt	Avail and/or Special
A-1	

# LIST OF TABLES

<u>TABLES</u>		<u>PAGE</u>
I	Calculated Infiltration Rates of Aluminum/Aluminum Alloys in SiC Capillaries for $r = 75\mu\text{m}$ , $\lambda = 10^{-2}$ , and $\xi = 0.5$ . . . . .	10
II	Characterization of the 100 Grit Green $\alpha$ -Silicon Carbide . . . . .	20
III	Comparison Between Experimental and Calculated Infiltration Rates and Pressures for Aluminum/Aluminum Alloys into SiC Compacts . . . . .	36

## THE INFILTRATION OF ALUMINUM IN SILICON CARBIDE COMPACTS

### 1.0 INTRODUCTION

Although metal matrix composites have been fabricated by various techniques, the most successful are solid state processes such as powder metallurgy and diffusion bonding [1]. Liquid metal processes such as compucasting, pultrusion, and infiltration, while less successful, are potentially more economical. Moderate success has been experienced by adding ceramics to the melt prior to casting and directly infiltrating the ceramic preforms [2]. The primary obstacle to the liquid metal techniques is the poor wettability of ceramics which results in flocculation, voids at interfaces and incomplete infiltration [3]. Degradation of the fiber by the infiltrant is likewise a problem [4,5].

Compucasting [6], a liquid metal process wherein a ceramic powder is stirred into a melt at a temperature between the liquidus and the solidus, appears to reduce flocculation. Having the consistency of a slurry, the partially solidified melt can mechanically entrap and react with the silicon carbide to form an interfacial bond. Composites produced by this process have been characterized by voids and poor bonding at the interface. Pressure (squeeze) casting has also been applied [7] to the liquid metal infiltration of SiC fibers with some success.

The advantages of producing silicon carbide-aluminum matrix composites by liquid metal infiltration techniques can not be fully realized without an improved understanding of the infiltration behavior and the fiber/matrix bonding mechanisms. Previous investigations [8,9], focusing on the effects of processing parameters such as pressure,

temperature, and alloying, were insufficiently complete to provide that understanding. This can only be achieved by analysis of the fundamental aspects of the process and confirmation of these concepts by experimentation. This paper reports on infiltration models which consider the physical properties of the liquid and preform (either porous compact or capillary/tube bundle). These properties include viscosity, density, surface tension, and wettability (pore shape and size in the case of the porous compact). The models have been assessed in terms of their ability to predict infiltration behavior from known physical properties of the materials.

## 2.0 DIMENSIONLESS SOLUTION FOR CAPILLARY RISE - WETTING SYSTEM

A kinetic approach was first developed by Brittin [10,11] for the rate of rise of a liquid in a capillary. For a wetting system, the interfacial tensions act to drive the liquid up the capillary while resistances to this motion such as gravitational, viscous, and end-drag forces act to drive the liquid down the tube. This is presented schematically in Figure 1. The resulting change in momentum due to these forces is:

$$\frac{d}{dt} m(t) \frac{dh}{dt} = F_{\gamma} + F_g + F_{\eta} + F_{ed} \quad (1)$$

where  $m(t)$  is the mass of the liquid in the capillary at time  $t$ ,  $F_{\gamma}$  is the force due to surface tension,  $F_g$  is the force due to gravity,  $F_{\eta}$  is the force due to viscous resistance,  $F_{ed}$  is the force due to end-drag and  $h$  is the height of infiltration at time  $t$ . The above



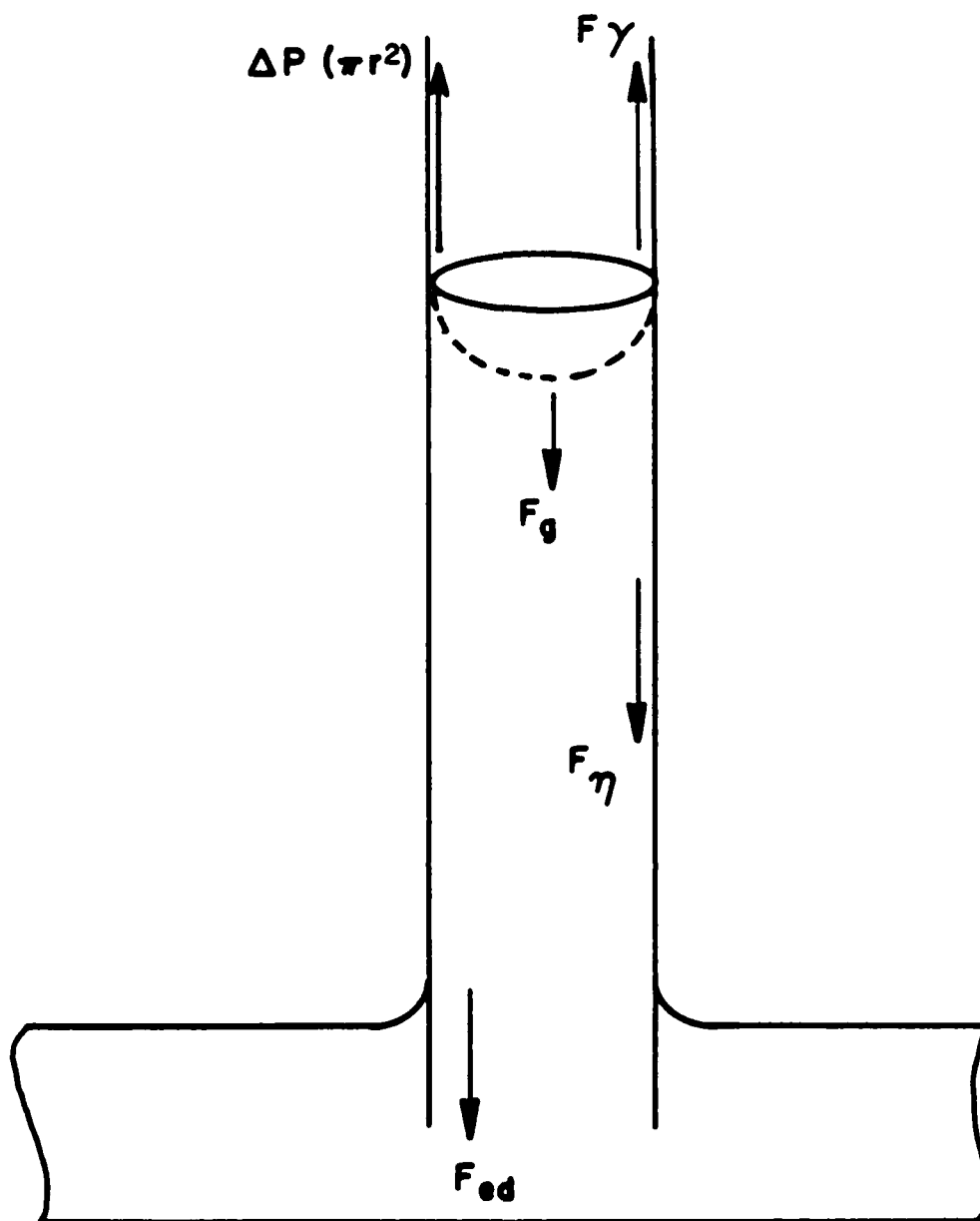


Figure 1. Schematic of forces balance for capillary rise

equation can be rearranged, after substitution, into the "dynamical differential equation" shown below:

$$h \left( \frac{d^2 h}{dt^2} \right) + \frac{5}{4} \left( \frac{dh}{dt} \right)^2 + ah \left( \frac{dh}{dt} \right) + gh = b \quad (2)$$

$$\text{where } a = \frac{8h}{\rho r^2} \quad ; \quad b = \frac{2 \gamma_{LV} \cos \phi}{\rho r}$$

Since an exact solution to the differential equation cannot be found, a dimensionless form of the equation was solved numerically with the following assumptions: (1) dominating viscous shear forces, (2) "small" infiltration heights, and (3) "short times" of infiltration. The results of the numerical solution for capillary rise in a wetting system are as follows:

$$t = \frac{16 \tau_2 \eta \gamma_{LV} \cos \theta}{g^2 \rho^2 r^3} \quad (3)$$

where:

$$\tau_2 = \frac{1}{2} \left( \frac{\xi^2}{1 - \xi} \right) \quad \text{-- DIMENSIONLESS TIME}$$

$$\xi = \frac{4.9 \text{ rph}}{\gamma_{LV} \cos \theta} \quad \text{-- DIMENSIONLESS HEIGHT}$$

$$\lambda = 1.15h \left( \frac{\gamma_{LV} \cos \theta}{r^5 \rho^3} \right)^{1/2}$$

The term  $\lambda$  delineates two limiting systems; for  $\lambda < 10^{-2}$ , inviscid flow predominates and for  $\lambda > 10^2$ , viscous flow predominates. In typical metal systems, the latter condition (viscous flow), predominates.

This approach for a wetting system was applied for both a tube bundle or capillary geometry as well as a porous compact geometry. Semlak and Rhines [12] also used this approach in their infiltration studies of porous-metal bodies. In their approach, the porous metal body was regarded as a tangled bundle of tubes with irregular radii. An "effective radius" was defined which could then be determined experimentally.

### 3.0 TUBE BUNDLE/CAPILLARY RISE EXPERIMENTS (NON-WETTING SYSTEM)

One of the two experimental approaches for investigating infiltration kinetics is based on a tube bundle or capillary geometry. For a non-wetting system, such as liquid aluminum and SiC, the liquid meniscus in a capillary will not rise up the tube but will in fact be depressed below the liquid level, as shown in Figure 2. By measuring the unperturbed equilibrium height of the meniscus in a capillary, both the liquid/vapor surface tension and contact angle can be determined. In the event a force or pressure is applied to overcome the negative surface tension force and drive a non-wetting liquid up a tube, the dynamics of the system can be studied. Both static and dynamic capillary rise experiments are currently being used to study the infiltration kinetics of the aluminum/SiC system. Once the infiltrated samples have been prepared, a destructive test will be used to determine bond strengths, in accordance with the previously proposed model [13].

$$\gamma_{LV} \cos \theta = \frac{r \rho g h}{2}$$

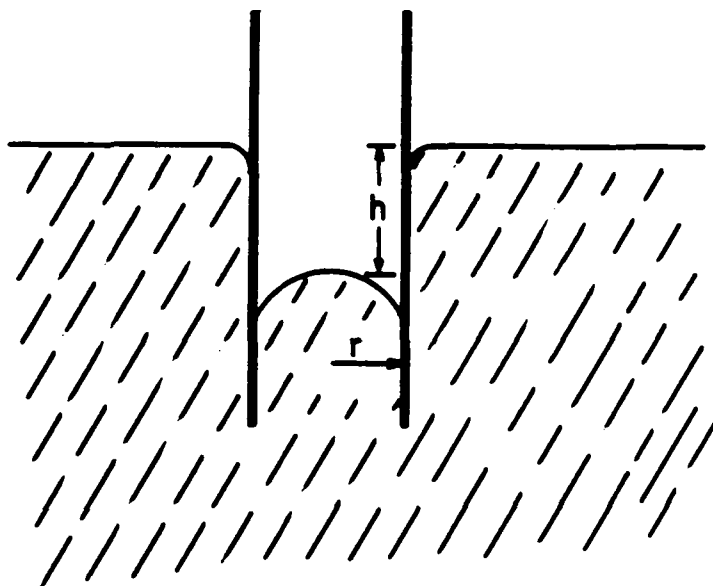


Figure 2. Capillary rise (non-wetting).

### 3.1 Static Measurements

In a static non-wetting system, the liquid meniscus in a capillary can be represented as shown in Figure 2. The equilibrium height,  $h$ , can be related to  $\gamma_{LV} \cos \theta$  by the LaPlace and Young equation, where:

$$\gamma_{LV} \cos \theta = \frac{r\rho gh}{2} \quad (4)$$

$\gamma_{LV} \cos \phi$  was determined for different aluminum alloys in contact with 1/8-in.-diam.  $\alpha$ -SiC tubes. The results for these tests are shown in Figure 3.

Each point in Figure 3 is an average of more than 5 successive measurements of the equilibrium height. In the first height measurement, for a given set of conditions, liquid aluminum was exposed to an as-received  $\alpha$ -SiC tube. The aluminum was removed and then repeatedly exposed to the same pre-wetted  $\alpha$ -SiC tube. The results from this technique for all the conditions shown in the figure indicate that there was no appreciable variation in the static height measurement with time or surface condition. These results also show that:

- 1) Wetting tendency of aluminum alloys, as a function of alloy additions, decreases in the order:  
 $\text{Al-2 wt \% Li} > \text{Al-2 wt \% Mg} > \text{Al-2 wt \% Si} > \text{Pure aluminum}$
- 2)  $\gamma_{LV} \cos \theta$  (wetting tendency) increases with increasing temperature (exception with bismuth)

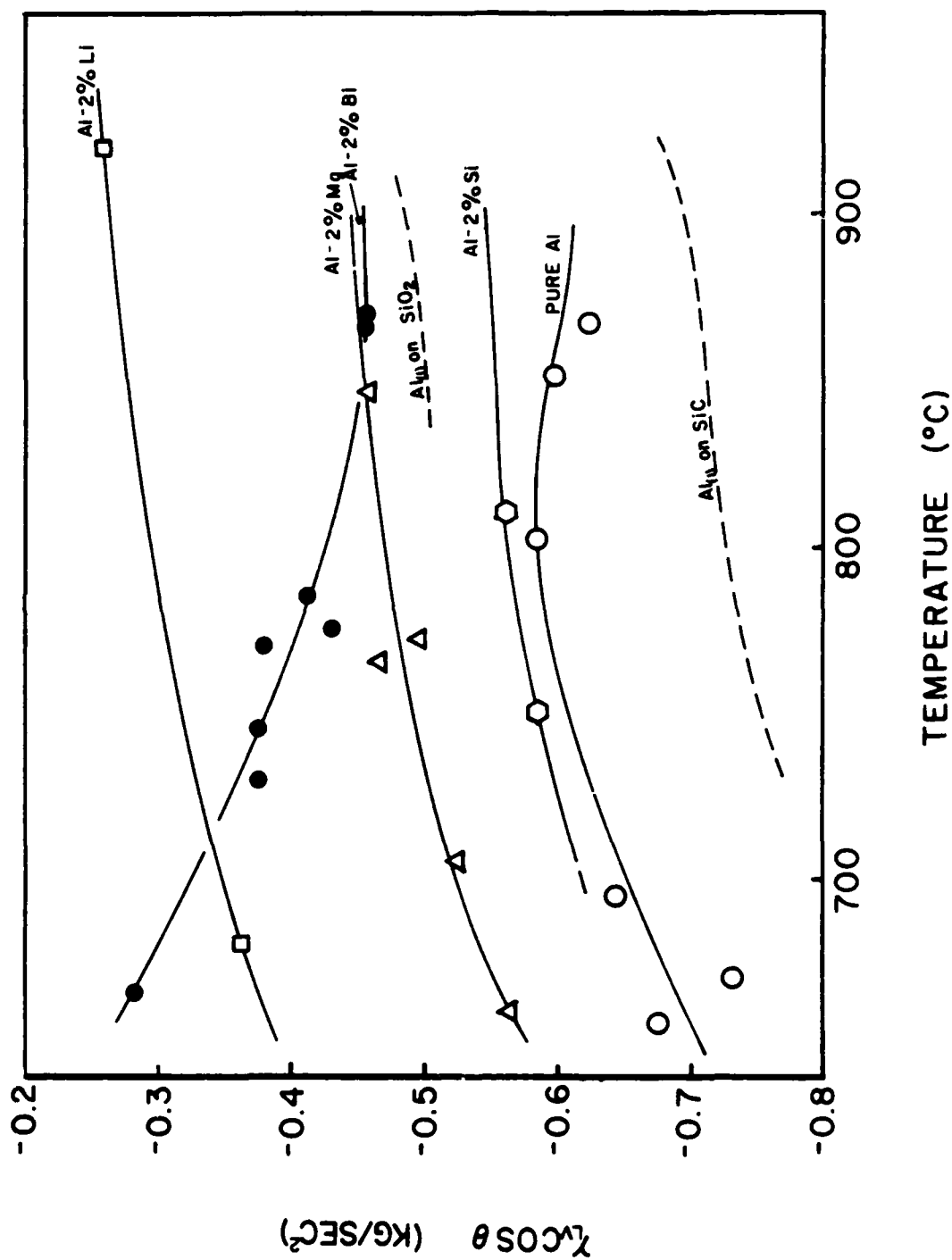


Figure 3. Wetting tendency ( $\chi_L \cos \theta$ ) versus temperature for various aluminum alloys on SiC.

- 3) Values of  $\gamma_{LV} \cos \phi$  for aluminum on as-received  $\alpha$ -SiC are between those for a pure Al/SiC system and those for a pure Al/SiO<sub>2</sub> system.

### 3.2 Dynamic Infiltration Rate Measurements

To overcome the negative surface tension force in a non-wetting system and get infiltration to occur, an applied force or pressure is needed. Referring to the following differential equation for liquid rise up a vertical capillary tube (wetting system)

$$h \left( \frac{d^2h}{dt^2} \right) + \frac{5}{4} \left( \frac{dh}{dt} \right)^2 + ah \left( \frac{dh}{dt} \right) + gh = b \quad (5)$$

an applied pressure term,  $\Delta P$ , can merely be added onto the constant term,  $b$ , on the right side of the equation. The magnitude of this applied pressure will be some fractional amount greater than  $b = 2 \gamma_{LV} \cos \theta / r$ . Upon combining the  $\Delta P$  term with the constant  $b$  term, the solution to this differential equation will be the same as that for the wetting case presented earlier. Calculated infiltration rates for aluminum into a SiC capillary with radius =  $75 \mu\text{m}$ ,  $g = 10^2$ , and  $\xi = 0.5$ , are shown in Table I. Note that the predicted infiltration times for the aluminum/lithium alloy are less than those for pure aluminum. The  $\gamma_{LV} \cos \theta$  values listed are from the previous static measurements.

TABLE I - Calculated Infiltration Rates of Aluminum/Aluminum Alloys in SiC Capillaries for  $r = 75\mu\text{m}$ ,  $\lambda = 10^{-2}$ , and  $\xi = 0.5$

INFILTRANT	TEMP ( $^{\circ}\text{C}$ )	$\rho$ <sub>3</sub> (g/cm <sup>3</sup> )	$\gamma\cos\theta_2$ (Kg/sec <sup>2</sup> )	$\Delta P$ (mmHg)	h (M)	t (sec)
PURE ALUMINUM	694	2.35	0.63	162	0.11	12.4
	851	2.29	0.585	150	0.105	12.1
ALUMINUM (+ 2%Li)	680	2.165	0.353	98	0.094	8.12
	920	2.124	0.25	76	0.09	6.0



An experimental apparatus is currently being built to measure infiltration rates of molten metals into capillary/tube bundle type geometries. A schematic of the apparatus is shown in Figure 4. The graphite crucible, containing molten metal, will be enclosed within a high purity argon atmosphere. In addition, to minimize contamination by any residual oxides on the molten metal surface onto the inside of the capillary, high purity argon can be blown through the tube to displace the oxides as the capillary tube is lowered into the melt (this argon will also purge the molten metal). The fine bore capillaries will be constructed by pressing an axially grooved 1/8-in.-diam. rod (i.e., splined shaft) into a 1/8-in. I.D. tube; each grooved valley in the rod will delineate a capillary and the tips of the ridges which press into the tube wall will separate each capillary.

After the SiC capillaries have been infiltrated with aluminum, the interfacial bond strength will be determined. Using the splined shaft core as a die, the shaft can be punched out of the tube. The resulting shear stress measurement will be correlated to the bond strength. The bond strength values obtained in this phase of the study can then be used to compare to the theoretical bond strength values that are determined from electronic material properties a model which has been proposed in previous work [13].

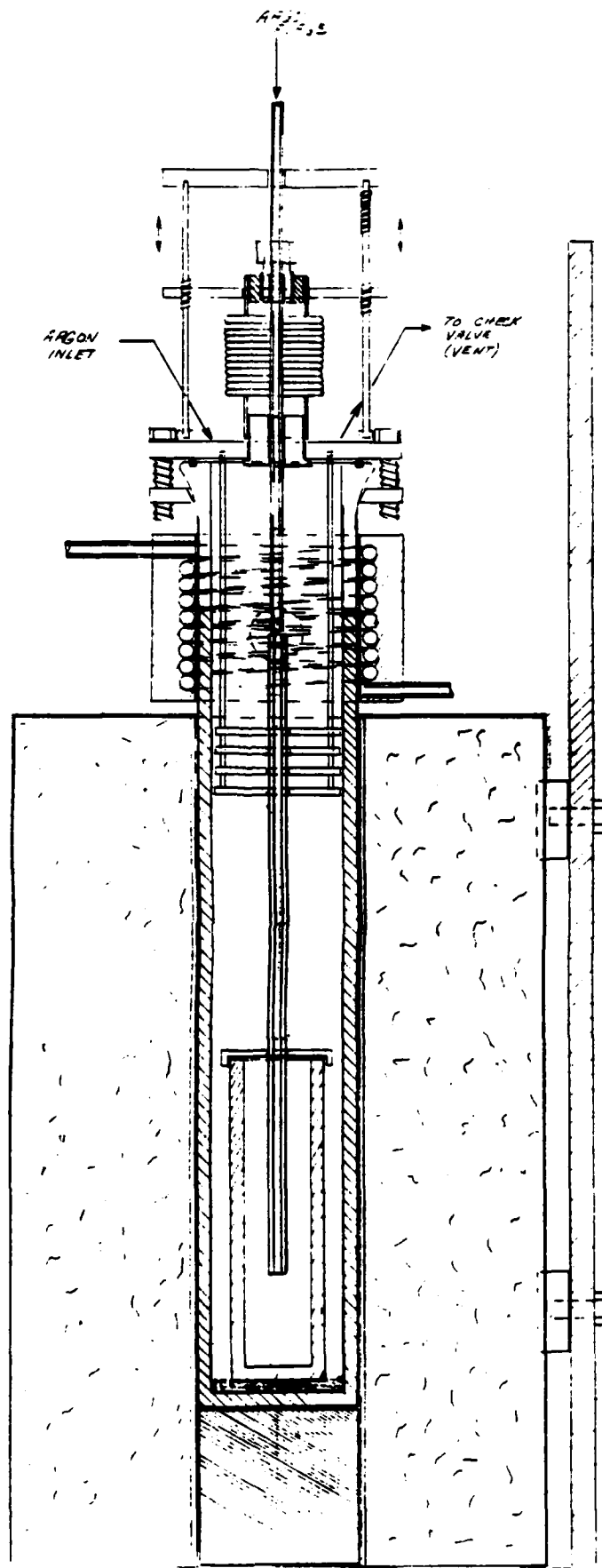


Figure 4. Schematic of experimental apparatus for capillary rise.

#### 4.0 POROUS COMPACT - NON-WETTING SYSTEM

##### 4.1 Theoretical Model

Another parallel approach to understanding the non-wetting Al/SiC system utilizes a porous compact geometry. The following model was developed for this study which involves a non-wetting system. Since pressure must be applied to induce infiltration in such a system, it was decided, on the basis of simplicity, to measure the flow rate at which the liquid aluminum flows downward through a silicon carbide powder compact. A schematic describing this model is presented in Figure 5. The dimension  $h$  is the distance the liquid has infiltrated at time  $t$ ,  $A_c$  is the cross sectional area of the compact,  $r_c$  is the radius of the compact,  $r_h$  is the effective pore radius (hydraulic radius),  $d_p$  is the particle diameter, and  $\theta$  is the void fraction. The origin is at the interface between the reservoir and the compact, with the positive direction being that in which the fluid is forced to flow.

The force balance for this model is:

$$F_P + F_g + F_\eta = \frac{d}{dt} \left[ m(t) \frac{dh}{dt} \right] \quad (6)$$

The primary difference between this force balance and that developed by Brittin [10] is that the end-drag and surface tension forces appear as part of a pressure related force,  $F_p$ , which also accounts for the applied pressure and the hydrostatic pressure.

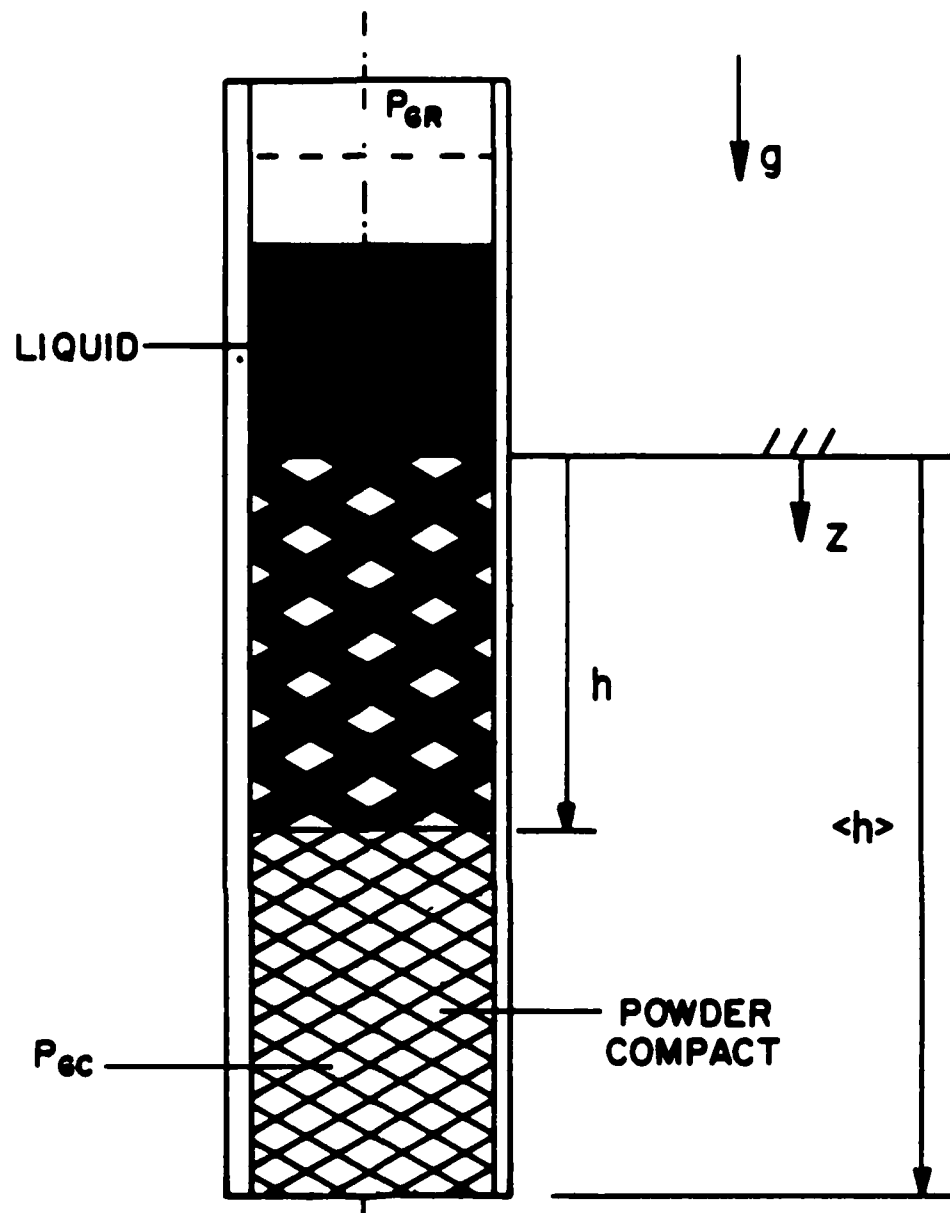


Figure 5. Schematic of porous compact sample geometry.

This force is related to the pressure drop across the porous body by:

$$F_P = \Delta P \phi A + F_Y - F_{ed} + F_H \quad (7)$$

$$\Delta P = P_{Gr} - P_{Gc} \quad (8)$$

where  $P_{Gr}$  is the applied pressure in the reservoir and  $P_{Gc}$  is the gas pressure within the compact. The pressure drop across the compact is then:

$$\frac{1}{\phi A} (F_P) = P_{GR} - P_{GC} + \frac{2 \gamma_{LV} \cos \theta}{r_h} + \rho g h_r + \rho \left( \frac{dh_c}{dt} \right)^2 \quad (9)$$

The viscous resistance to a fluid flowing through a powder compact can be developed by applying the equation, first utilized by Semlak and Rhines [12], for flow through a tube:

$$F_\eta = -\frac{\phi A_c}{r_h} 8\eta h_c \frac{\phi h_c}{dt} \quad (10)$$

The result is:

$$F_h = -\phi A_c \left[ K_1 \eta h \left( \frac{dh}{dt} \right) + K_2 \rho h \left( \frac{dh}{dt} \right)^2 \right] \quad (11)$$

where:

$$K_1 = \frac{150 (1 - \phi)^2}{\phi^2 d_p^2} ; K_2 = \frac{1.75 (1 - \phi)}{\phi^2 d_p} \quad (12)$$

The gravitational force acting upon the liquid within the compact is:

$$F_g = \phi A \rho g h \quad (13)$$

Equating the sum of the forces described above to the rate of change in momentum and dividing through by  $\phi A$  we obtain:

$$\begin{aligned} \rho \frac{d}{dt} (h_c \frac{dh}{dt}) = \Delta P + \frac{2\gamma_{LV} \cos \theta}{r_h} + \rho g h - \rho \left( \frac{dh}{dt} \right)^2 \\ - [K_1 \eta h \frac{dh}{dt} + K_2 \rho h \left( \frac{dh}{dt} \right)^2] + \rho g h \end{aligned} \quad (14)$$

where  $\Delta P = P_{GR} - P_{GC}$ . Infiltration will only occur if:

$$\Delta P + \frac{2\gamma_{LV} \cos \theta}{r_h} + \rho g h > 0 \quad (15)$$

The expression on the left defines the effective pressure,  $P_{eff}$ .

When  $P_{eff}$  is zero,  $\Delta P$  is equal to  $P_{th}$ , the threshold pressure, or an applied pressure that must be exceeded to initiate infiltration.

A dimensionless form of the above kinetic expression was solved numerically and the results are given below (for large  $\lambda_1$ ):

$$\frac{1}{2} \xi^2 = \tau / \lambda_1 \quad (16)$$

where:

$$\xi = \frac{h}{\langle h \rangle}$$

$$\tau = \left[ \frac{1}{\langle h \rangle} \left( \frac{P_{eff}}{\rho} \right)^{1/2} \right] t$$

$$\lambda_1 = \frac{K_1 h \langle h \rangle}{(\rho P_{eff})^{1/2}}$$

and  $\langle h \rangle$  is a reference height of some arbitrary value.

#### 4.2 Experimental Methodology

The infiltration kinetics model suggests that altering either pore morphology, viscosity, density, interfacial free energies, or applied pressure, will effect the infiltration rate. The properties selected for study were those associated with the liquid metal (i.e. surface free energies, density and viscosity). The

alloys selected, in addition to pure aluminum, were aluminum-1 wt % silicon and aluminum-1 wt % magnesium.

To minimize silicon carbide degradation, a temperature range near the melting point of the aluminum/aluminum alloys was selected. Since the viscosity of liquid aluminum and its alloys has been found to demonstrate a sharp increase as the melting point is approached, the temperature selected for comparing the alloys was 670°C, or 10°C above the melting point of aluminum. However, additional testing was performed on pure aluminum at both 3°C above 660°C (the melting temperature), and at 1050°C and on an aluminum-1 wt % silicon alloy at both 6°C above and 2°C below its liquidus temperature.

The tests at 1050°C were run for the following reasons. Below  $\approx$  950°C, reported [14] contact angles for the Al/SiC system are between 150° and 160° (i.e., non-wetting). At about 1050°C, the contact angle drops to 90° and above 1100°C, the contact angle levels out at about 30°. If the surface tension force was the only resistance to infiltration, then decreasing the contact angle to less than 90° should spontaneously promote infiltration. Hence, tests were run at 1050°C to investigate whether infiltration could occur spontaneously without an applied pressure.

For each alloy at each temperature, a threshold pressure was experimentally determined to within  $\pm$  3 kPa. The threshold pressure was defined as the minimum pressure necessary to initiate infiltration within a 30-minute interval. To study the effect of alloying on the infiltration kinetics, a large value of the



threshold pressure (98 kPa), was selected for comparison. Because this "comparison" pressure was above the threshold pressure for pure aluminum, a final series of pure aluminum tests were performed at 670°C with lower pressures. These final tests provided a means of demonstrating the effect of just pressure on the infiltration kinetics.

#### 4.3 Body Characterization

Application of the infiltration model requires values for void fraction, effective particle diameter, and effective pore radius. The last two quantities are not directly measurable for a body containing a mixture of particles with different sizes and shapes. However, if the void fraction is known, these dimensions can be derived experimentally by applying Ergun's Equation [15] to a system with established physical properties.

A 100 grit green  $\alpha$ -SiC powder was used in this entire infiltration study. Using a Jeol JXA 840 Electron Probe Analyzer, the size and shape factor distribution was evaluated and the results are presented in Table II.

The void fraction was determined by slowly adding water to silicon carbide powder compacts. The specimens were weighed before and after all the voids were filled with water, and the void fraction was calculated based on the water weight gain.

Pressure drop versus flow rate measurements were then obtained for argon flowing through silicon carbide compacts. The range of flow rates selected was such that the flow behavior would

TABLE II - Characterization of the 100 Grit Green  $\alpha$ -Silicon Carbide

Nominal Composition, wt. pct.					
<u>SiC</u>	<u>Si</u>	<u>SiO<sub>2</sub></u>	<u>C</u>	<u>Fe</u>	<u>Al</u>
98.65	0.15	0.63	0.36	0.08	0.08

Dimensional Analysis*		
<u>Parameter</u>	<u>Average</u>	<u>Std. Dev.</u>
Ave. Diameter( $\mu$ m)	47.73	24.08
Max. Diameter( $\mu$ m)	91.05	40.74
Min. Diameter( $\mu$ m)	25.97	17.57
Shape Factor	2.35	0.66

\*based upon 524 particles evaluated

be similar to that expected in the infiltration studies. This was determined by calculating the expected range of Reynold's numbers,  $R_e$ , for this study, and then determining the argon flow rates which would cover this range. The Reynold's number is given by:

$$Re = \frac{\rho V_o}{\eta(1-\phi)S_o} \quad (17)$$

where:

$$S_{o_p} = \frac{6}{d} \quad ; \quad V_o = \phi \frac{dh}{dt_c} = \frac{Q}{A} \quad (18)$$

and  $Q$  = volumetric flow rate. For the small flow rates of interest, only the viscous term in Ergun's equation is significant, and the equation can be simplified by eliminating the inertial term. The compressibility of argon must also be accounted for, making the applicable form of the equation as follows:

$$\frac{dP}{dl} = K_1 \eta \frac{G_o}{P} \left( \frac{RT}{M} \right) \quad (19)$$

where  $G_o$  is the mass flow rate ( $\rho Q/A_c$ ),  $R$  is the gas constant,  $T$  is the absolute temperature and  $M$  is the molar

weight. By integrating over the length of the compact, this becomes:

$$\frac{1}{2}(P_g + 2 P_g P_b) = K_1 \eta \frac{RT}{L_H} G_o \quad (20)$$

where  $P_g$  is the pressure at the top of the compact,  $P_b$  is the barometric pressure at the bottom of the compact, and  $L$  is the length of the compact.  $K_1$  can then be obtained from the slope of a plot of  $0.5 (P_g + 2 P_g P_b)$  versus  $G_o$ . Knowing  $K_1$  and  $\phi$ , the effective particle diameter can be calculated from the definition of  $K_1$ . Particle diameter  $d_p$  is then related to the effective pore radius by:

$$r_h = \frac{d_p \phi}{6 (1 - \phi)} \quad (21)$$

The flow rate of argon through three silicon carbide compact samples was measured over a range of pressure drops. The results are presented in Figure 6 along with data for the stainless steel screen. A linear regression analysis of these data was performed and the values of  $K_1$  were determined. The coefficient of determination for the data was found to be 0.964, indicating good linear correlation. Since the slope of the line is the resistance to flow, and since the compact and the screen act as resistors in series, the resistance due to the compact alone was obtained from the

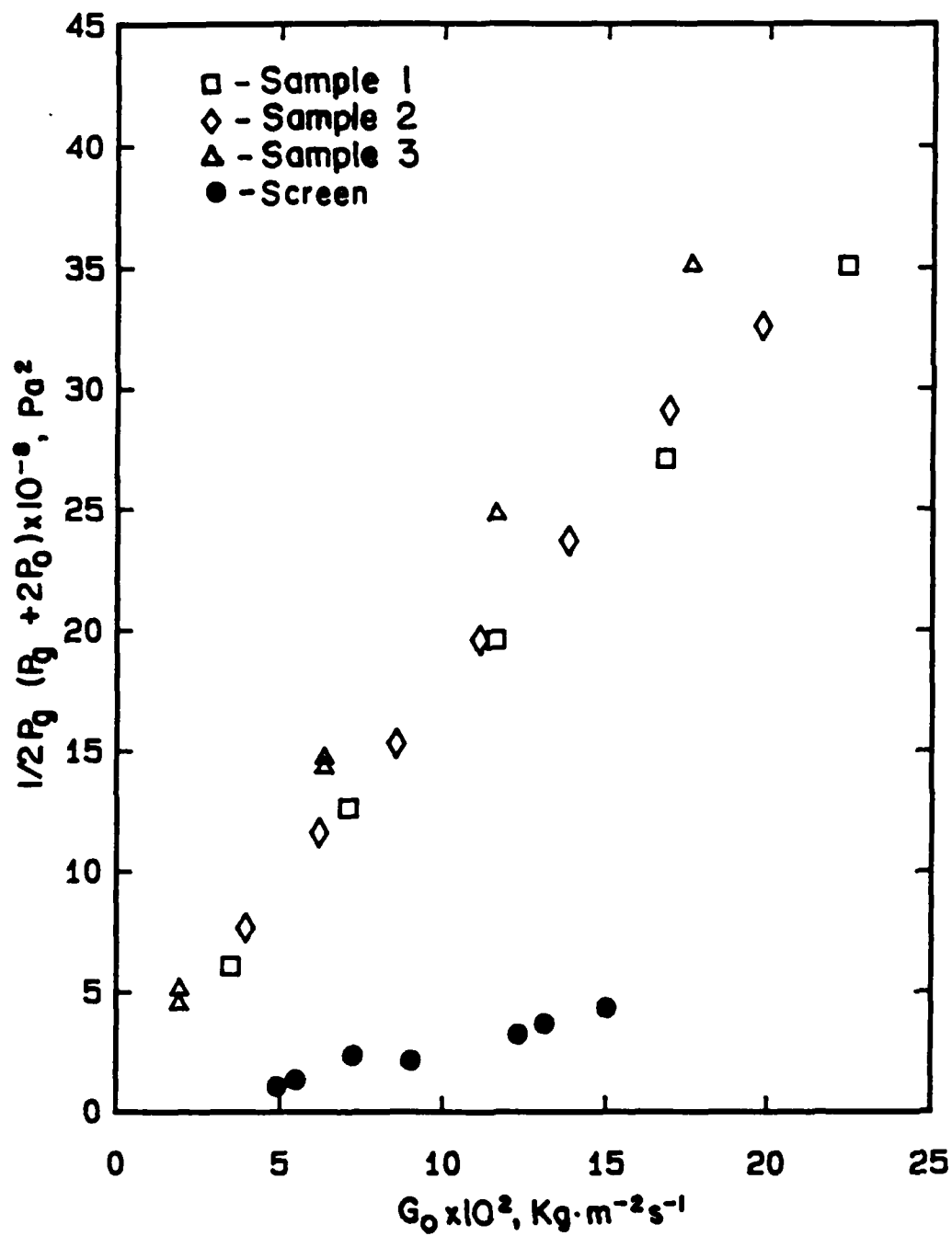


Figure 6. Plot of  $1/2 P_g (P_g + 2 P_0)$  versus flow rate for green SiC compact (100 grit).

difference between the slope of the line through the compact data and that of the screen. The value of  $K_1$  determined by this method was  $2.577 \times 10^{11} \text{ s}^{-3}$ .

Five compacts were evaluated for pore fraction. The average pore fraction was found to be 0.426, with a standard deviation of 0.007. Using this value in the equation for  $K_1$  resulted in a calculated value of  $32.6 \mu\text{m}$  for the effective particle diameter. This calculated value for  $K_1$  agreed well with the particle measurements performed on the scanning electron microscope. The effective pore radius was calculated to be  $4.02 \mu\text{m}$ .

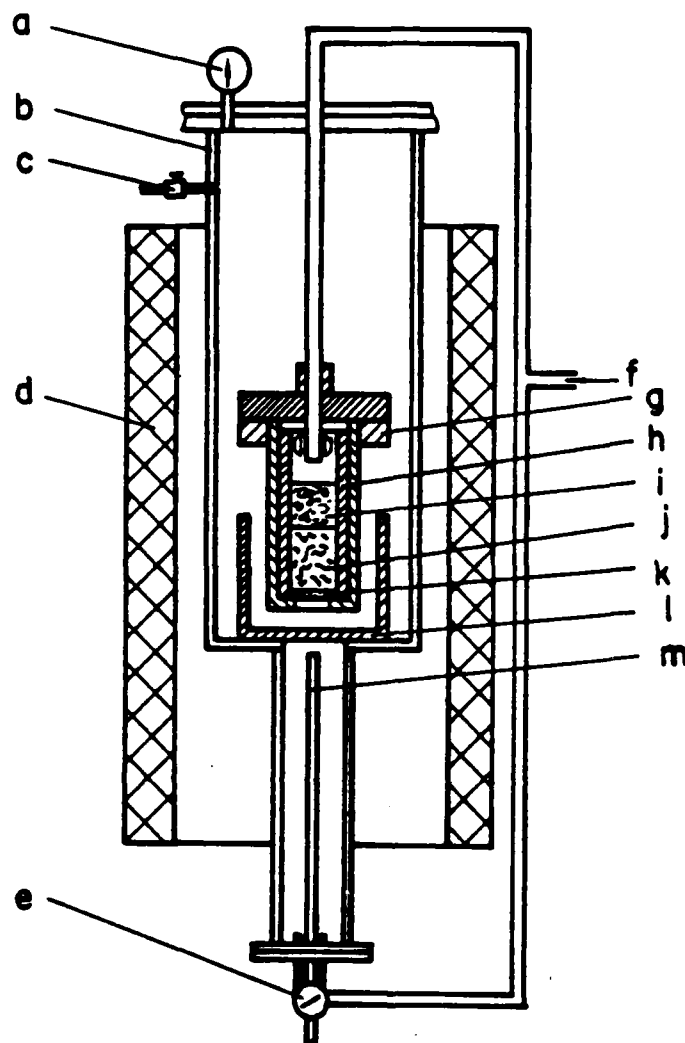
The above method, using Ergun's equation, works well for a fixed pore geometry. In the infiltration tests described in the next section however, it was found that the pore geometry does not remain fixed. As liquid infiltrates and penetrates into the pores, bouyancy and fluid flow shear forces rearrange the original pore configuration. Metallographic examination of the infiltrated samples has shown the pore volume fraction to be on the order of 0.80; an increase in pore volume of about 100% over the calculated uninfiltrated value of 0.43. It was also found in the infiltration studies that as the applied pressure was increased above the threshold, pressure liquid turbulence began to occur and the character of a porous compact deviated drastically from its original uninfiltrated condition.

Since the results from Ergun's method agreed well with experimental data for fixed pore geometries, it could be used in tests where the porous compacts are constrained or preformed, such as with sintered or bound.

#### 4.4 Infiltration Kinetics

##### 4.4.1 Procedure

The specimen arrangement within the furnace is presented in Figure 7. After a powder specimen was preloaded and packed into an alumina tube (12.5mm I.D. x 92.0mm long), an aluminum alloy plug was then packed on top of the powder (alloys were prepared with 99.95% purity aluminum). To assure temperature uniformity within the working zone, a tube furnace, with a high length to diameter ratio (9.1m long x 0.1m I.D.) was used. The furnace was heated directly to the selected temperature and allowed to stabilize. A specimen was then lowered into the working zone. While the specimen was equilibrating ( $\approx$  90 minutes), the gas pressure was increased to the value selected for the particular test. To initiate a test and create a pressure drop, the argon supply to the furnace chamber was valved off and the chamber vented to the atmosphere. At the end of a specified time, the vent was closed, the argon supply valve was opened, and the specimen was raised into the cold zone. After the specimen had cooled, it was forced from the alumina tube using a hydraulic press.



- a) Pressure Gage
- b) Chamber
- c) Vent
- d) Furnace
- e) Valve
- f) Argon
- g) Fixture
- h) Al<sub>2</sub>O<sub>3</sub> tube
- i) Aluminum
- j) Compact
- k) Screen
- l) Crucible
- m) Thermocouple

Figure 7. Schematic of experimental apparatus for porous compact.



The specimens were sectioned longitudinally, polished, and then analyzed. For each specimen, whether partially or fully infiltrated, an average infiltration time and distance was determined. Selected samples were observed with the SEM to characterize the aluminum alloy/SiC interfacial region.

#### 4.4.2 Results and Discussion

Data obtained from the infiltration experiments is presented graphically in Figures 8 to 13. As shown in Figures 8 and 9, increasing the applied pressure for pure aluminum at 670°C decreased the initiation time. At the 90% confidence level, no conclusion could be made as to whether pressure effected the infiltration rate after initiation.

Comparing the infiltration behavior at 670°C and 90 kPa for pure aluminum, an aluminum-1 wt % silicon alloy and an aluminum-1 wt % magnesium alloy (Figures 9, 11, and 12) indicated that: (1) all three alloys manifested an initiation time prior to liquid metal infiltration, and (2) addition of either silicon or magnesium increased the initiation time. This initiation time is most likely related to an interfacial reaction which is altering the capillarity force. As the interfacial reaction proceeds, the magnitude of the opposing interfacial force is reduced. At some point the set applied pressure overcomes the interfacial force, and infiltration commences.

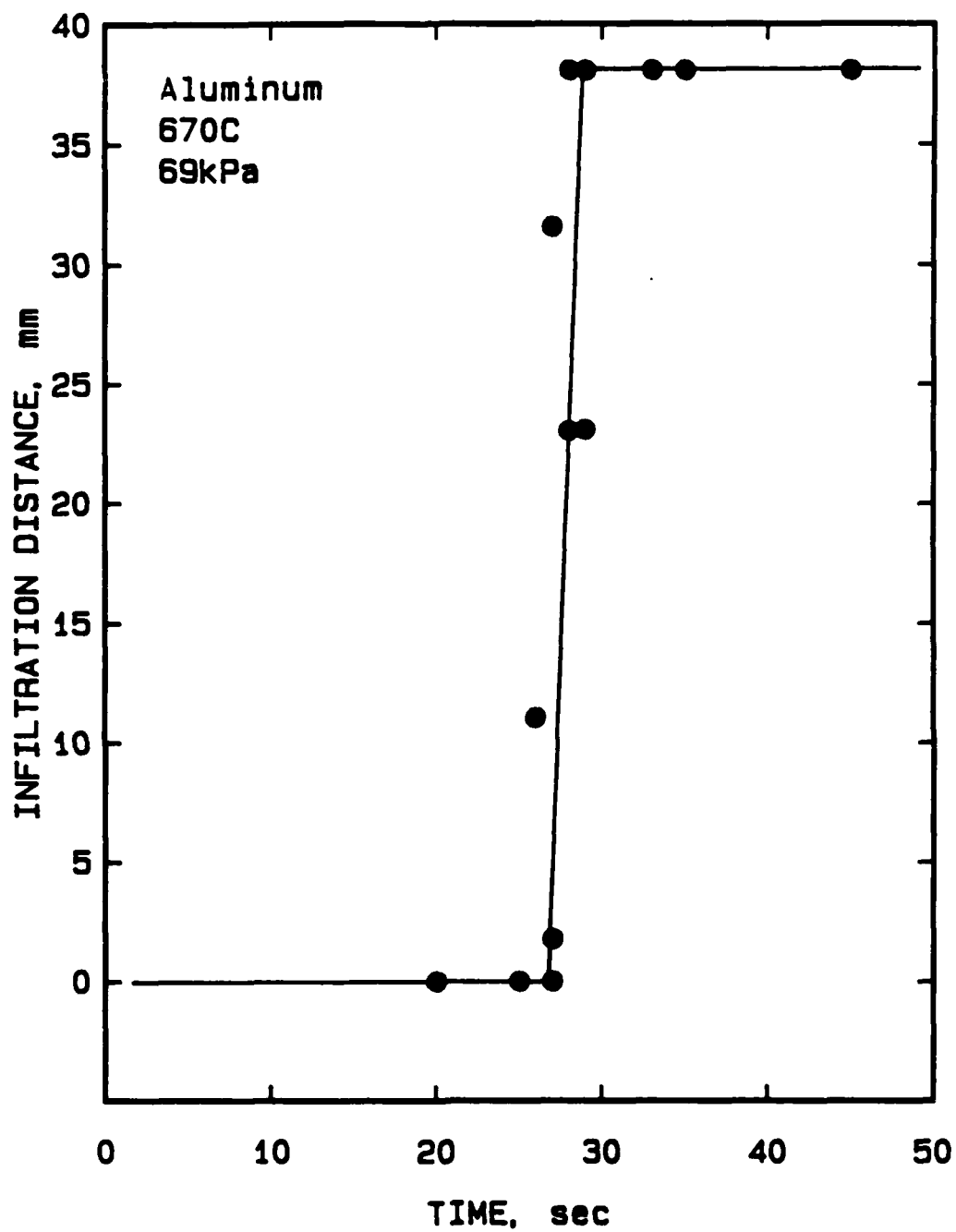


Figure 8. Infiltration distance versus time for aluminum in SiC at 670°C and 69 kPa.

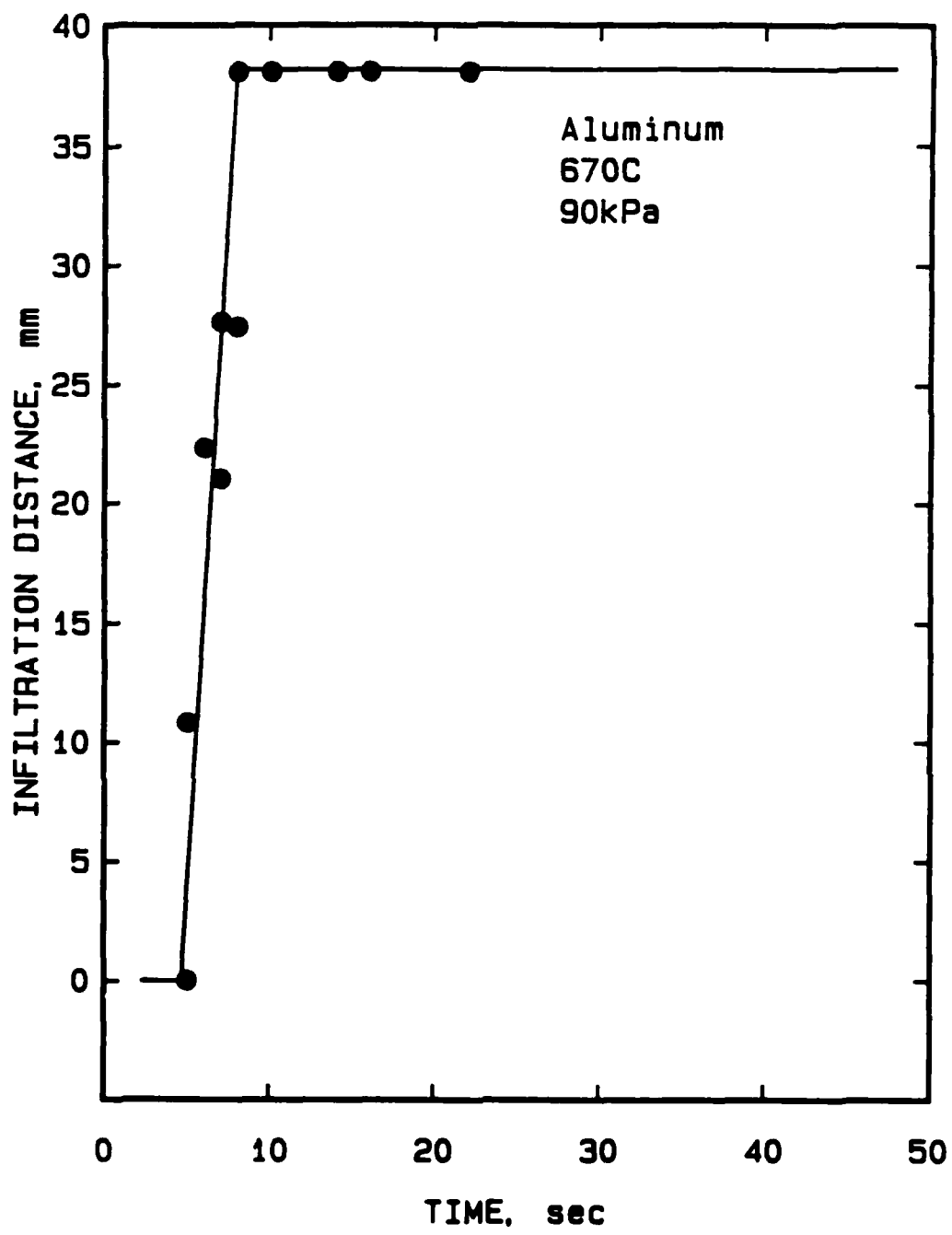


Figure 9. Infiltration distance versus time for aluminum in SiC at 670°C and 90 kPa.

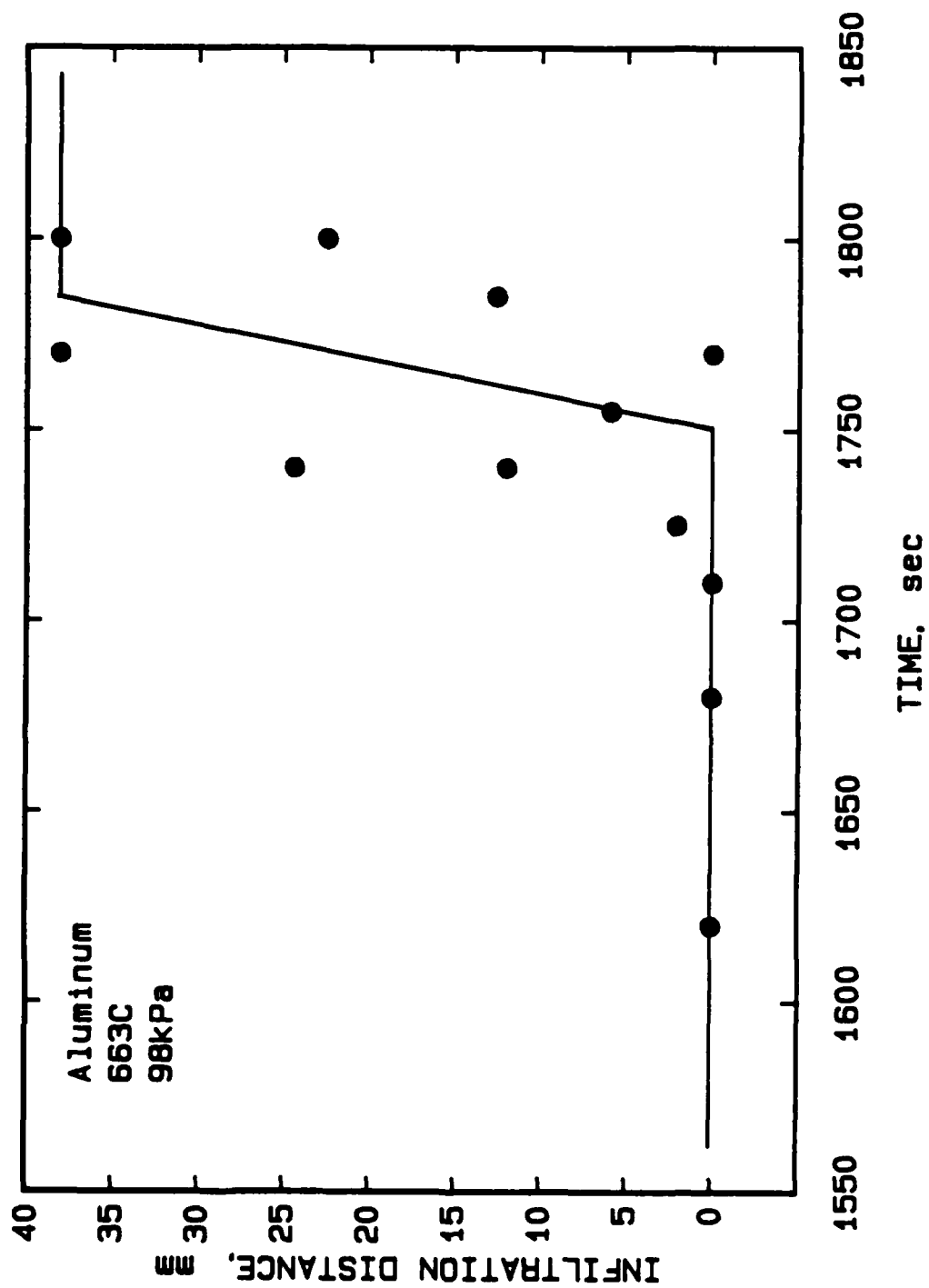


Figure 10. Infiltration distance versus time for aluminum in SiC at 663°C and 98 kPa.

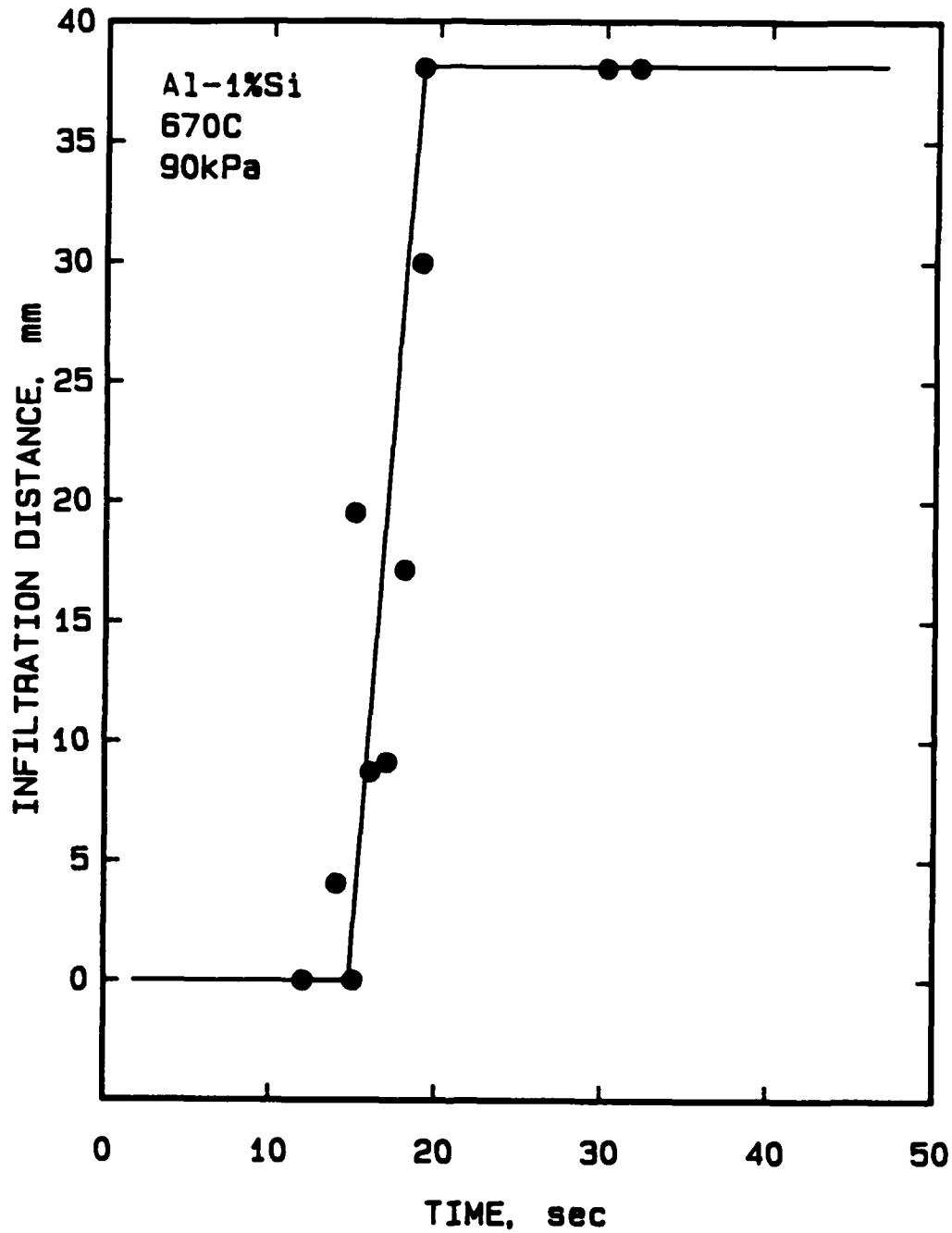


Figure 11. Infiltration distance versus time for aluminum-1 wt % silicon in SiC at 670°C and 90 kPa.

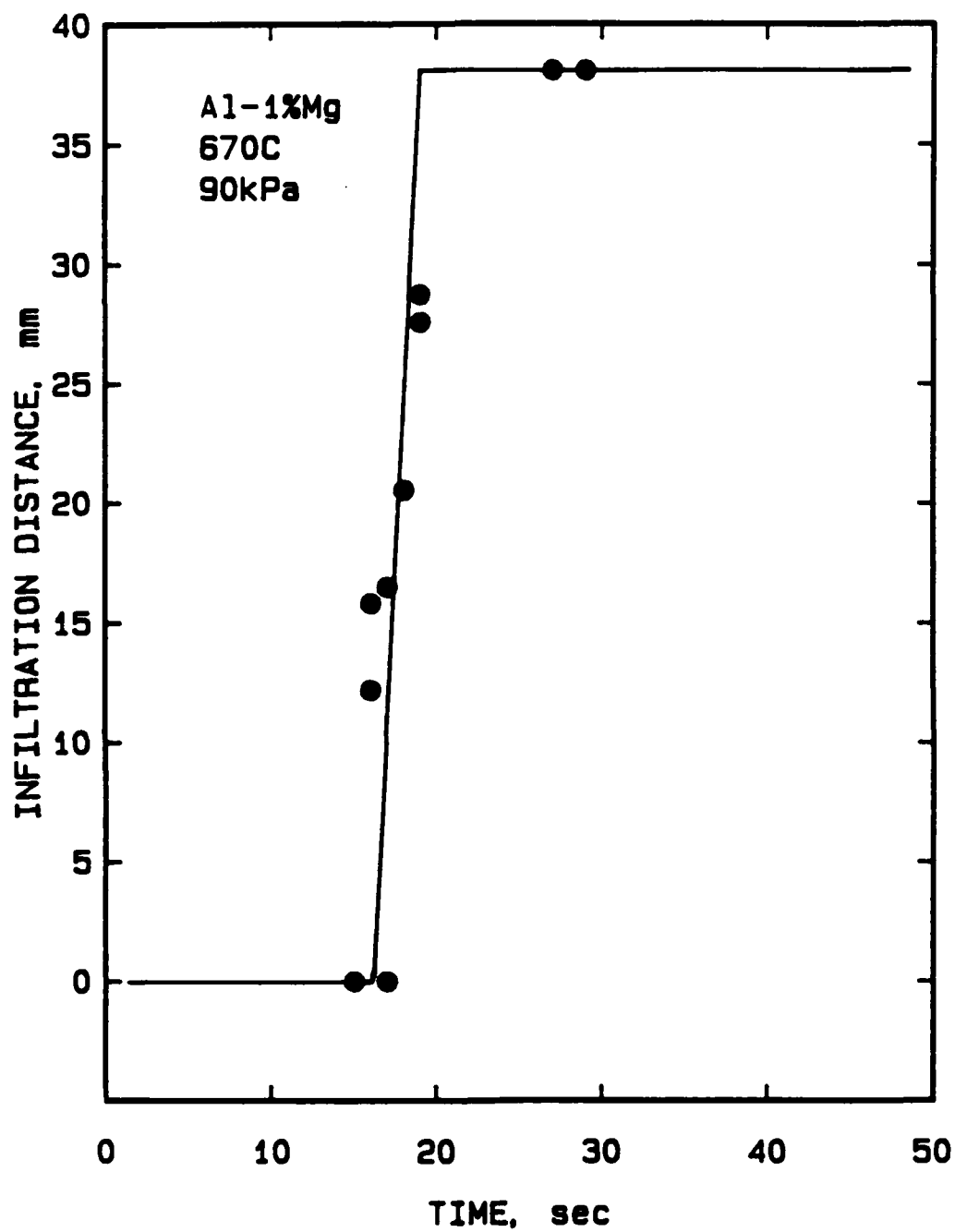


Figure 12. Infiltration distance versus time for aluminum-1 wt % Mg in SiC at 670°C and 90 kPa.

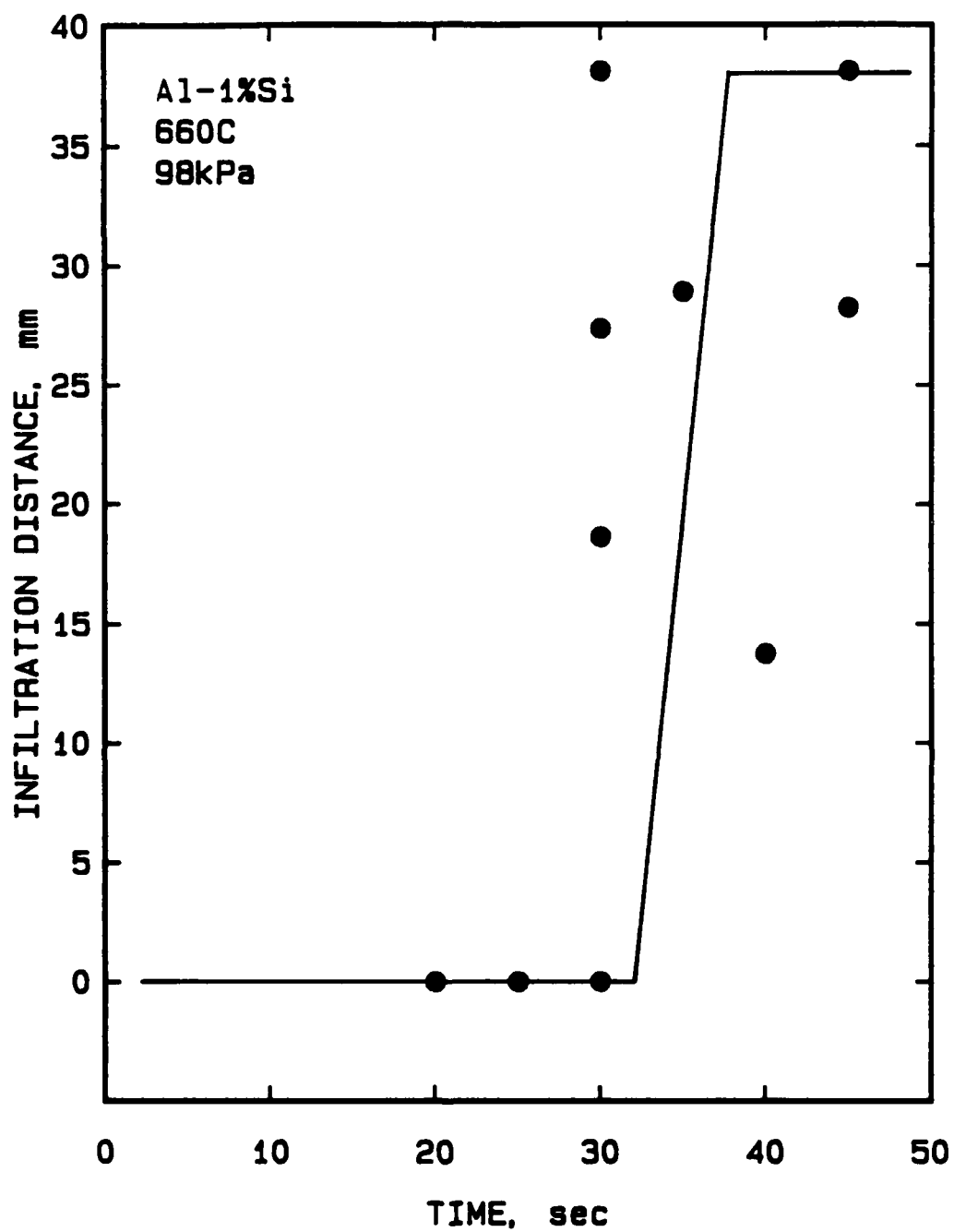


Figure 13. Infiltration distance versus time for aluminum-1 wt % Si in SiC at 660°C and 98 kPa.

Figures 9 and 10 for pure aluminum and Figures 11 and 13 for the aluminum-1 wt % silicon, show that a small reduction in temperature results in a major increase in the initiation time. This is even more significant when considering the fact that at the lower temperature, a higher applied pressure was used (98 kPa for aluminum at 663°C versus 90 kPa at the higher temperature). This suggests that the initiation time is related to a thermally activated interfacial reaction, such as the reaction of aluminum with the protective  $\text{SiO}_2$  layer on the SiC surface. As the surface reaction proceeds, the  $\gamma_{LV} \cos \theta$  decreases and infiltration can occur.

The tests run near the liquidus were characterized by long initiation times and large scatter bands. This behavior is consistent with the reported variability in viscosity data, which has been attributed to short range ordering prior to solidification. When the temperature was increased to 670°C, the threshold pressure for both the aluminum and aluminum-1 wt % silicon decreased. As shown in Figure 9 the effect was more pronounced with the aluminum.

The tests performed at 1050°C, without applied pressure, did not result in spontaneous infiltration even though the contact angle at this temperature has been reported to be less than 90° [14]. Other factors, such as interfacial reaction kinetics, or fluid flow end effects may have prevented infiltration. Comparison between experimental



and calculated infiltration rates are shown in Table III. Since particle rearrangement occurred in these tests, Ergun's method could not be used to calculate void fractions and particle diameters on uninfiltrated compacts. With the aid of an optical microscope, a point count method was devised for determining the void fractions directly from the infiltrated samples. An average void fraction of 0.80 was determined, and an effective pore radius of  $21.7\mu\text{m}$  was recalculated using Ergun's relation.

Although the infiltration rates were consistently higher (and the threshold pressures consistently lower) than expected, the infiltration rates calculated for the systems tested near their threshold pressures (i.e., pure aluminum at  $670^{\circ}\text{C}$  and  $69^*\text{ kPa}$ ), are within the 90% confidence intervals of the experimental results. At larger values of the effective pressure,  $P_{\text{eff}}$ , the differences in the experimental and calculated results can not be accounted for by experimental error. These discrepancies are undoubtedly caused by changes in the flow behavior and the compact particle rearrangements occurring at high applied pressure.

#### 4.4.3 Conclusions

- 1) Pressure is required to initiate infiltration of silicon carbide powder compacts with aluminum within the temperature range of  $660^{\circ}\text{C}$  to  $1050^{\circ}\text{C}$ .

TABLE III - Comparison Between Experimental and Calculated Infiltration Rates and Pressures for Aluminum/Aluminum Alloys into SiC Compacts

Alloy	Temp(°C)	P* (kPa)	Experimental		Calculated**		P <sub>th</sub>
			$\frac{dh}{dt}$	$\frac{mm}{sec}$	$\frac{dh}{dt}$	$\frac{mm}{sec}$	
Aluminum	670	90		11		113	71
Al-1Si	670	90*		9		19	71
Al-1Mg	670	90		11		96	67
Aluminum	670	69*		25		19	71
Aluminum	663	98*		1		17	71
Al-1Si	660	98*		6		17	71

\* denotes threshold pressure(+3.5/-0). P<sub>th</sub> for Al-1Mg at 670°C is 72kPa

\*\* calculations based upon  $\phi = 0.8$  and  $\theta = 155^\circ$

- 2) The pressure required for infiltration changes with alloying. Alloying with either 1 wt % silicon or 1 wt % magnesium was found to increase this pressure; silicon was found to cause the greatest pressure increase.
- 3) The pressure required for infiltration decreases with increasing temperature.
- 4) An initiation time is associated with the infiltration of silicon carbide compacts with aluminum. This initiation time decreases with increasing pressure and temperature.
- 5) Within a 90% confidence interval, the measured rates agreed with the calculated rates for effective pressures at or slightly above the threshold pressures.
- 6) For effective pressures much greater than the threshold pressures, the inconsistencies between the measured and calculated rates were the result of extensive particle redistribution.

## 5.0 FUTURE WORK

### 5.1 Capillary/Tube Bundle Experiments

Future work will include both static and dynamic measurements of infiltration parameters for various alloys and alloy compositions in both the Al/SiC and Mg/Graphite systems. The samples prepared in the above infiltration experiments will then be tested with either a punch/die shear technique or nano-indenter

technique to determine bond strengths. Finally, measurement of the electronic material properties will be used to correlate the initial infiltration rate to the ultimate bond strength in accordance with the proposed model.

## 5.2 Porous Compact Experiments

Initially, work will continue to complete the time-temperature-pressure correlation presented earlier. This will include an investigation into the reproducibility of measured infiltration rates. As part of this investigation, both the effect of particle size and distribution and constrained versus unconstrained compacts will be studied. The major scope of this work will then be directed at understanding the relation between interfacial reactions and incubation time; this may involve controlling the solidification by controlling the interfacial reaction region.

## 6.0 ACKNOWLEDGMENTS

The mathematical modeling reported herein was performed by Dr. Gerald Martins, and his contributions to this work are gratefully acknowledged. The efforts of Research Assistants Paul Maxwell and Bruce Lanning were also crucial to this research.

## 7.0 REFERENCES

1. Toth, I.J., Brentnall, W.D., and Menke, G.D., "Fabricating Aluminum Matrix Composites", J. Metals, 24, pp. 19-25 (1972).
2. Clyne, T.W. and Bader, M.G., "Analysis of a Squeeze-Infiltration Process for Fabrication of Metal Matrix Composites", Fifth Intern. Conf. on Comp. Mater.: ICCM-V, San Diego, pp. 755-771 (1985).
3. Banerji, A., Rohatgi, P.K. and Reif, W., "Role of Wettability in the Preparation of Metal-Matrix Composites (A Review)", Metallwissenschaft Technik, 38, pp. 656-661 (1984).
4. Cornie, J.A., Mortensen, A., Gunger, M.N. and Flemmings, M.C., "The Solidification Process During Pressure Casting Sic and  $Al_2O_3$  Reinforced Al-4.5% Cu Metal Matrix Composites", Fifth Intern. Conf. on Comp. Mater.: ICCM-V, San Diego, pp. 809-823 (1985).
5. Ackermann, L., Charbonnier, J., Desplanches, G. and Koslowski, H., Properties of Reinforced Aluminum Foundry Alloys", Fifth Intern. Conf. on Comp. Mater.: ICCM-V, San Diego, pp. 687-698 (1985).
6. Mehrabian, R., Riek, R.G. and Flemmings, M.C., "Preparation and Casting of Metal-Particulate Non-Metal Composites", Met. Trans. 5, pp. 1899-1905 (1974).
7. Sakamota, A., Hasegawa, H., and Minoda, Y., "Mechanical Properties of SiC Whisker Reinforced Aluminum Composites", Fifth Intern. Conf. on Comp. Mater.: ICCM-V, San Diego, pp. 699-707 (1985).
8. Clyne, T.W., Bader, M.G., Cappleman, G.R., and Hubert, P.A., "The Use of a  $\delta$ -Alumina Fibre for Metal-Matrix Composites", J. Mat. Sci. 20, pp. 85-96 (1985).

9. Hosking, F.M., and Netz, A.A., Liquid Metal Infiltration of an Aluminum Alloy into a Packed Column of B,C Particles, Research Report, Sandia National Laboratory, (1984).
10. Brittin, W.E., "Liquid Rise in a Capillary Tube", J. App. Phys., 17, pp. 37-44 (1946).
11. Ligenza, J.R. and Bernstein, R.B., "The Rate of Rise of Liquids in Fine Capillaries", J. Am. Chem. Soc., 73, pp. 4636-4638 (1951).
12. Semlak, K.A., and Rhines, F.N., "The Rate of Infiltration of Metals", AIME Trans., 212, pp. 325-331 (1958).
13. Edwards, G. R., et al., "Modeling of Infiltration Kinetics and Interfacial Bond Strength in Aluminum Matrix-Silicon Carbide Composites", Annual Report, ONR Contract No. N00014-85-K-0451 (1986).
14. Kohler, W., "Untersuchungen zur Benetzung von  $Al_2O_3$  und SiC-Kristallendurch Aluminum und Aluminiumlegierungen", 51, pp. 443-447 (1975).
15. Geiger, G. H. and Poirier, D. R., Transport Phenomena in Metallurgy, Addison-Wesley Publishing Co., London, pp. 94-98 (1973).

END

10-87

DTIC